ACS OMEGA

Open Access

http://pubs.acs.org/journal/acsodf

Article

Decomposition Model of Bastnaesite and Its Fluorine Oxygen Coupling Escape Mechanism

Jianfei Li, Yubo Xu, Xiaowei Zhang, Jinxiu Wu, Zhisheng Dong, Zhaogang Liu,* and Xiaoyan Hao

Cite This: *ACS Omega* 2024, 9, 38437−38451

Read Online

ACCESS | Metrics & More | Article Recommendations

ABSTRACT: Nearly 90% of rare earths worldwide currently originate from bastnaesite ($REFCO_3$). Oxidative roasting, an effective method for the treatment of bastnaesite, has been extensively employed in industrial production practice. However, the roasting decomposition mechanism of bastnaesite at the molecular level remains controversial. In this study, two roasting atmospheres (i.e., Ar and O_2) were adopted for the treatment of the mixed rare earth concentrate in Bayan Obo. Ar-Roasting ore was skillfully treated as an intermediate and then underwent oxidation roasting. The results achieved using research methods (e.g., XRD, FT-IR, TEM, and XPS) first revealed that the oxidation roasting of bastnaesite was performed in several stages. The first stage was the thermal decomposition of bastnaesite and the oxidation of cerium ($REFCO_3 \rightarrow REOF + CO_2$). The second stage was the escape pathway of fluorine ($REOF + O_2 \rightarrow RE_xO_y + O_xF$ and $O_xF \rightarrow O_2 + F_2$), describing the migration rules of F and O elements and the oxidation behavior of Ce. The results of this study can provide more theoretical support and guidance for the clean extraction of bastnaesite and mixed rare earth in Bayan Obo.

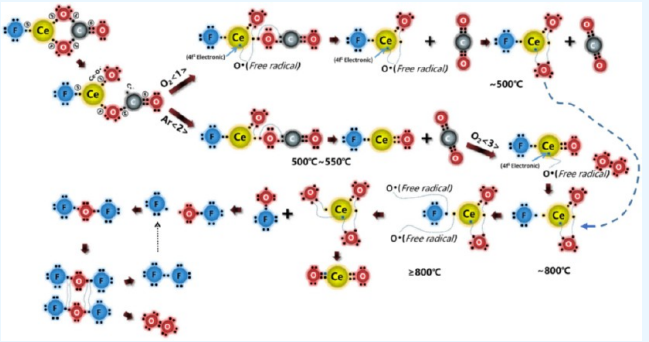

1. INTRODUCTION

Rare earth has been confirmed as a nonrenewable and vital strategic resource.[1] Rare earth elements have been extensively employed in numerous highly sophisticated fields, especially in aerospace and military products that take on critical significance in a wide range of countries[2−4] since these elements exhibit a special electron layer structure and numerous prominent physical and chemical properties from the macroscopic perspective.[5] Currently, the global sources of rare earth are mainly concentrated in more than 10 kinds of rare earth minerals with industrial mining value (e.g., bastnaesite ($REFCO_3$), monazite ($REPO_4$), xenotime (YPO_4), yttrium fluorite (Ca, Y)F_2, $[Al_2Si_2O_5(OH)_4]_m$-REO, and (Ce, La)$_2Ca_2(CO_3)F$),[6] and bastnaesite, monazite, and xenotime account for over 90% of the global supply of rare earth;[7] bastnaesite has been confirmed as one of the critical raw materials in the global rare earth industrial production for its superior smelting performance, huge reserves, and simple process, and its rare earth recovery rate is capable of directly determining the global rare earth supply chain.[8]

In general, oxidative roasting is taken as the first step of the technical route in the recent industrial production of bastnaesite.[9−11] After oxidation roasting, bastnaesite (with rare earth carbonate covered) can be decomposed into rare earth compounds that are more soluble in acid. Subsequently, most of the rare earths can be transferred into a solution through an acid leaching process, such that rare earths can be efficiently leached.[12,13] The roasting process has been reported as a more mature method, and it has been extensively employed in rare earth production practices. Nevertheless, a considerable number of key issues remain about the transformation of the mineral phase of bastnaesite during roasting, comprising how O_2 plays a certain role in the reaction, how the chemical bond of fluorine is broken, how to achieve controlled regulation of the roasting product, and the redox behavior of Ce^{3+}/Ce^{4+} that have not been precisely described,[14] coupled with the fact that most studies only use economic indicators (e.g., rare earth recovery and leaching rate) to examine the merits of the process, resulting in a lack of deeper understanding of the reaction mechanism in the roasting of bastnaesite, and the roasting mechanism has not been studied in depth. The roasting process of bastnaesite has not been capable of achieving a revolutionary change over the past few years.

It is generally believed that bastnaesite will decompose to form CeOF, CO_2, and other phases (eq 1) in the roasting

Received: March 3, 2024
Revised: July 9, 2024
Accepted: July 26, 2024
Published: September 6, 2024

process,[15−18] but it is difficult to explain the escape of small amounts of F and the oxidation of Ce in the process.[12] Several scholars suggested that bastnaesite will decompose to form CeO_2, CO_2, and F_2 (eq 2), whereas CeO_2 will continuously decompose to CeO_{2-X} and O_2 (eq 3) when heated.[19,20] As indicated by recent research, the generated CeOF will continue to react with CO_2 to form CeO_2, CeF_3, and CO (eq 4). Subsequently, CeO_2 and CO continuously undergo redox reactions to form Ce_2O_3, CO_2, and so on (eq 5).[21] As indicated by existing research, there is still no unified conclusion on the roasting products and the roasting reaction mechanism of bastnaesite, and some of the above-mentioned research processes are only at the conjectural stage, with no definite evidence of the generation of gases such as F_2 and CO. For this reason, research on the roasting reaction mechanism of bastnaesite can provide a theoretical reference and take on critical significance in the research and development of the rare earth industry.

Bayan Obo mixed rare earth ore serves as a vital source of bastnaesite, and its high-temperature roasting reaction process is more sophisticated.[22,23] For this reason, a Bayan Obo mixed rare earth concentrate was employed as a raw material to explore the roasting reaction process of its bastnaesite, gain insights into the mechanism of fluorine and oxygen coupling and the oxidation behavior of Ce, infer the reaction process and element migration law, and provide a certain reference for promoting the clean production of the Bayan Obo mixed rare earth concentrate in depth.

$$CeFCO_3 \rightarrow CeOF + CO_2 \quad (1)$$

$$CeFCO_3 + O_2 \rightarrow 2CeO_2 + 2CO_2 + F_2 \quad (2)$$

$$CeO_2 \rightarrow CeO_{2-x} + \frac{x}{2}O_2 \quad (3)$$

$$CeOF + CO_2 \rightarrow CeO_2 + CeF_3 + CO \quad (4)$$

$$CeO_2 + CO \rightarrow Ce_2O_3 + CO_2 \quad (5)$$

2. EXPERIMENTS

2.1. Raw Materials and Reagents. The rare earth concentrate used in this study was obtained from China Northern Rare Earth (Group) Hi-Tech Co., Ltd., and the chemical compositions and rare earth contents of the sample are listed in Table 1.

Table 1. Chemical Analysis of Mixed Rare Earth Concentrates

REO (%)	F (%)	P (%)	CaO (%)
62.38	8.23	2.54	6.45

2.2. Experimental Methods and Test Methods. The raw material employed in this study was a Bayan Obo mixed rare earth concentrate, which was primarily composed of bastnaesite and a small amount of monazite (with rare earth grade of 65%; Ce accounted for over 50% of the rare earth allocation). The mixed rare earth concentrate was employed after sieving and drying (80 °C, 2 h). Figure 1 presents a schematic diagram of the research scheme. In this study, the changes in a series of physical phases and product structures of the rare mixed earth concentrate were mainly investigated in different roasting atmospheres (O_2/Ar), the reaction process was predicted, and the roasting reaction mechanism was speculated. There were three main roasting processes, which are elucidated below.

1. In the research on the Ar-roasting process, a box was customized to avoid and reduce the effect of residual O_2 in the furnace chamber on the roasted products in the roasting process. Six layers of the mixed rare earth concentrate of identical mass were placed. Next, the packet was placed in an atmospheric furnace. The sample was evacuated to a furnace pressure of −0.04 MPa. Afterward, Ar was introduced to a furnace pressure of the standard atmosphere, and then, the sample was evacuated again to a furnace pressure of −0.04 MPa. We cycled the process three times following the aforementioned steps. The final pressure gauge display value should be −0.04 MPa. Afterward, we ensured precise control of conditions such as roasting time and temperature. After the preset conditions were reached, the product was cooled to ambient temperature and removed, and the product was termed Ar-roasting ore. Figure 1 shows the Ar-roasting ore in an Ar-roasting atmosphere at 550 °C.
2. In the research on the O_2-roasting process, the atmosphere was air, and the mixed rare earth concentrate was directly roasted and then decomposed in a high-temperature furnace to prepare the product termed O_2-roasting ore.
3. In this study, Ar-roasting ore was cleverly considered as an intermediate product, and the Ar-roasting ore was then oxidized and roasted (the second roasting method) to prepare the product termed O_2−Ar-roasting ore.

The TG-DSC curve was generated using a thermogravimetric analyzer (STA-449C) from Netzsch, Germany. XRD phase analysis was conducted using an X-ray diffractometer (D8 ADVANCE) from Bruker, Germany. The group or chemical bond breakage of the sample was analyzed through Fourier transform infrared spectroscopy (Nicolet iS50) from Thermo Fisher, US. The chemical valence states of Ce, F, O, and other elements in the sample were explored through X-ray photoelectron spectroscopy (ESCALAB 250Xi) from Thermo Fisher, US. The adsorption of O_2 on the sample was examined using a chemical adsorption instrument (PCA-1200) from Beijing Pioneer Company. The pyrolysis gas was analyzed with an online mass spectrometer (HPR-20) from Ingehead, UK. The diffraction ring of the sample was analyzed and then characterized under a Japanese transmission electron microscope (JEM-2100F).

3. RESULTS AND DISCUSSION

3.1. XRD and TG-DSC Analysis. Figure 2 presents the XRD patterns of the mixed rare earth concentrate. As depicted in Figure 2, the mixed rare earth concentrate primarily comprised bastnaesite-Ce (●-$CeFCO_3$), monazite-Ce (▼-$CePO_4$), apatite (■-$Ca_5(PO_4)_3F$), fluorite (▲-CaF_2), thorianite (◆-$Pb_{0.875}Th_{0.125}F_{2.25}$), cerianite-Ce (☆-$Ce_{0.33}Th_{0.33}La_{0.33}O_{1.83}$), and other phases. While rare earth minerals largely covered bastnaesite and monazite, bastnaesite served as the most abundant mineral in the mixed rare earth concentrate. The significant difference in the thermal decomposition behaviors of bastnaesite and monazite can lay a solid basis for the study of the roasting reaction mechanism of bastnaesite in the mixed rare earth concentrate

https://doi.org/10.1021/acsomega.4c02088
ACS Omega 2024, 9, 38437−38451

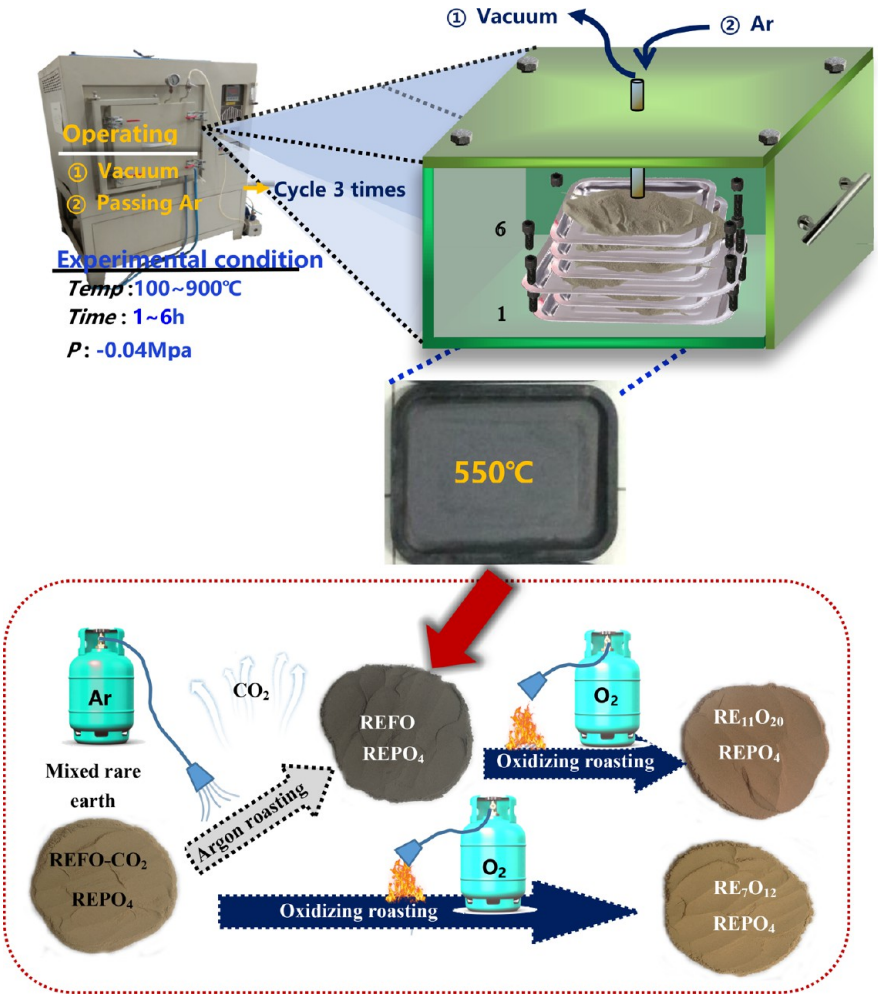

Figure 1. Schematic diagram of the research scheme (exploring the reaction mechanism of bastnaesite through the regulation of different roasting atmospheres).

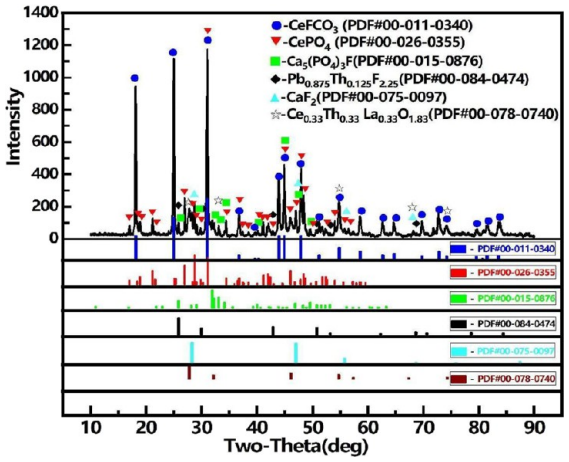

Figure 2. XRD patterns of the mixed rare earth concentrates (the test conditions: 2°/min, copper target).

from Bayan Obo. Accordingly, the above mixed rare earth concentrates were roasted in different roasting atmospheres, and their physical phase structure changes and evolution patterns were examined.

Figure 3 illustrates the XRD patterns of Ar−O_2-roasting ore, Ar-roasting ore, and O_2-roasting ore. As depicted in Figure 3, the main phases of Ar−O_2-roasting ore comprised $Ce_{11}O_{20}$, $Ce(PO_4)$, CaF_2, $Ca_2F(PO_4)_3$, and $Ce_{0.33}Th_{0.33}La_{0.33}O_{1.83}$. The valence state of Ce in the most abundant $Ce_{11}O_{20}$ ranged from +3 to +4, with an average value of +3.32, and no F element played a certain role in bonding. The main phases of Ar-roasting ore comprised $Ce_3O_4F_3$, $Ce(PO_4)$, CaF_2, $Ca_5F(PO_4)_3$, and $Ce_{0.33}Th_{0.33}La_{0.33}O_{1.83}$. The average valence state of Ce in the most abundant $Ce_3O_4F_3$ was +3.66, whereas elemental F played a significant role in bonding. The main phases of O_2-roasting ore covered Ce_7O_{12}, $Ce(PO_4)$, CaF_2, $Ca(PO_4)_3$, and $Ce_{0.33}Th_{0.33}La_{0.33}O_{1.83}$. The average valence state of Ce in the most abundant Ce_7O_{12} reached +3.43, and no F element played a certain role in bonding. After the main peaks of the three calcined ores were magnified, the result indicated that the relative angular offsets of the four main peaks of $Ce_{11}O_{20}$, Ce_7O_{12} and the four main peaks of $Ce_3O_4F_3$ reached 0.92, 0.43° (b1-a1, b1-c1), 1.17, 0.56° (b2-a2, b2-c2), 1.22, 0.60° (b3-a2, b3-c2), and 1.71 and 0.88° (b4-a4, b4-c4), respectively. Accordingly, Ar-roasting ore may serve as one of the intermediate products in the roasting process of bastnaesite, and O_2 may facilitate the oxidation of Ce^{3+} while causing the escape of F.[24]

The weight loss rate and TG-DSC data of the O_2-roasting ore and the O_2−Ar-roasting ore were identified (Figure 4) to verify the above conjecture. As depicted in Figure 4a, with the

https://doi.org/10.1021/acsomega.4c02088
ACS Omega 2024, 9, 38437−38451

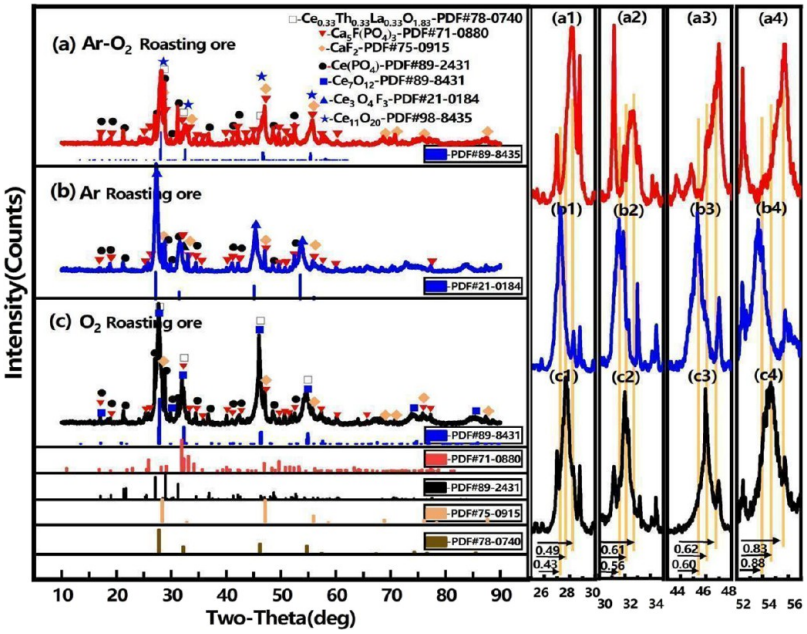

Figure 3. XRD analysis of mixed rare earth concentrates under different roasting atmospheres: (a) Ar−O_2-roasting ore, (b) Ar-roasting ore, and (c) O_2-roasting ore (the test conditions: 2°/min, copper target).

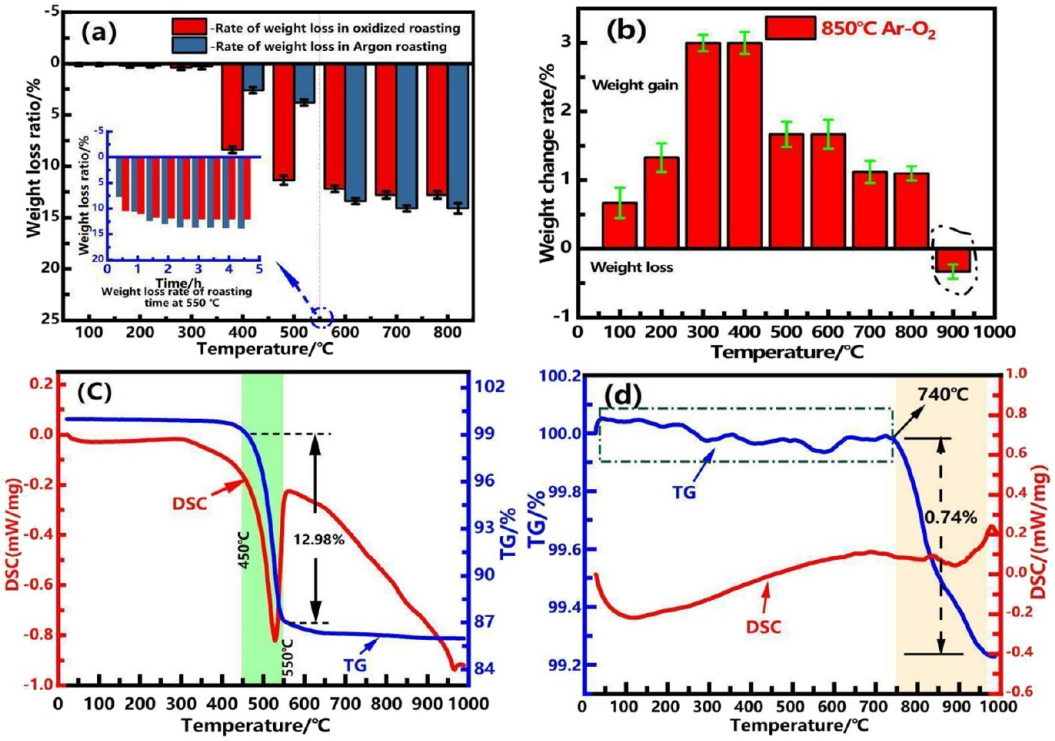

Figure 4. Weight loss rate and TG-DSC. (a) Weight loss rate of O_2-roasting ore (red lines) and Ar-roasting ore (blue line), (b) weight loss rate of O_2−Ar-roasting ore, (c) TG-DSC of O_2-roasting ore, and (d) TG-DSC of O_2−Ar-roasting ore.

gradual increase of the roasting temperature, the O_2-roasting ore had a significant weight at nearly 500 °C with a weight loss rate of 11.36%, consistent with the results presented in Figure 4c. The possible reason for this result is the release of CO_2. In contrast, the argon roasting started extensive decomposition only at 550 °C, about 50 °C higher than the oxygen roasting temperature, consistent with the literature results.[21] Accordingly, the involvement of O_2 will be conducive to reducing the decomposition temperature of bastnaesite. Moreover, to try to avoid experimental errors arising from unreacted CO_3^{2-}, the Ar-roasting ore at 850 °C was selected for the oxidation roasting test again (Figure 4b). As indicated by the result, with the gradual increase of the roasting temperature (100−400 °C), the weight of the O_2−Ar-roasting ore tended to be increased. The possible reason for this result is that the free radical O· in air gradually filled the remaining oxygen vacancies and defects of $Ce_3O_4F_3$ while causing the transformation of Ce^{3+} to Ce^{4+}. During this transformation, the adsorption of

https://doi.org/10.1021/acsomega.4c02088
ACS Omega 2024, 9, 38437−38451

free radical O· exceeded the escape. At the roasting temperature of ≥500 °C, although the weight gain phenomenon was still notable, the weight gain ratio tended to decline. This study suggested that the escape of free radical O· was increased at this time, and its ability to fill oxygen vacancies gradually decreases. The above finding was an important reason why CeO_2 exhibits excellent oxygen storage and release capacity and has been extensively used in catalysis.[25] When the roasting temperature was increased to >800 °C, a significant weight loss was identified, and the weight loss rate was about 0.33%, probably attributed to the escape of O or F from $Ce_3O_4F_3$. Although this result differed from the decomposition temperature at which the weight loss began in Figure 4d by nearly 50 °C, this can be attributed to the reabsorption of some of the radical O· in the cooling process with the furnace in Figure 4b. It is noteworthy that the TG curve (blue) of Figure 4d displayed irregular fluctuations in the range of 100−800 °C with an exothermic tendency. The above-mentioned result may suggest that the adsorption and escape of free radical O· during low-temperature roasting may be in a dynamic equilibrium.

The structure of O_2−Ar-roasting ore phases at different temperatures was analyzed in depth to further explain the weight gain and weight loss changes exhibited by O_2−Ar-roasting ore during roasting. As depicted in Figure 5, with the

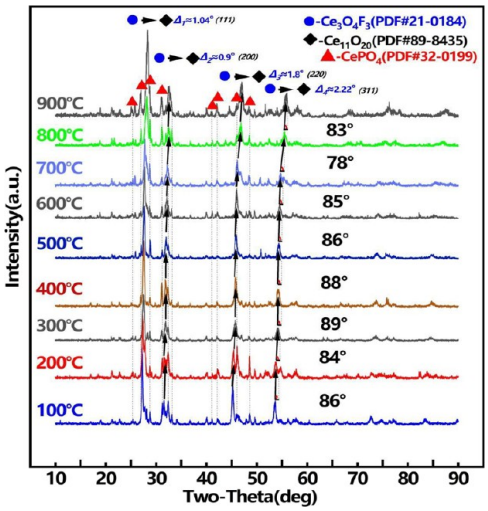

Figure 5. XRD diagram of O_2−Ar-roasting ore at different roasting temperatures.

increase of the roasting temperature, the rare earth physical phase then gradually shifted from $Ce_3O_4F_3$ (●) to $Ce_{11}O_{20}$ (◆), while the main diffraction peaks of the (111), (200), (220), and (311) crystalline surfaces shifted to higher angles with the offset (Δ) of nearly 1.04, 0.9, 1.8, and 2.22°, respectively. The possible reason for this result is that the ionic radius of oxidation of Ce^{4+} (0.092 nm) is smaller than that of Ce^{3+} (0.1034 nm),[26] resulting in a decrease in the cell parameters. Notably, the offset angle was the smallest (78°) when the roasting temperature was elevated from 700 to 800 °C, and a gradual broadening of the diffraction peak was identified, suggesting that the phase transition was most significant at this stage, consistent with the results in Figure 4b,d. As revealed by the in-depth analysis of O_2 adsorption by Ar-roasting ore, Ar-roasting ore exerted a certain adsorption effect (Figure 6), thus confirming that Ar-roasting ore can have more oxygen vacancies, such that the adsorbed O_2 is the root cause of Ce^{3+} oxidation.

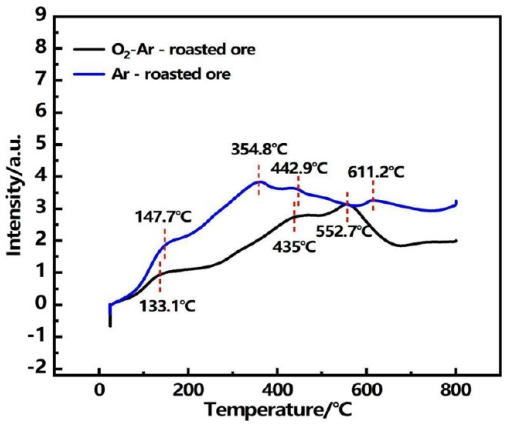

Figure 6. O_2 adsorption test (the blue line represents the adsorption of oxygen by Ar-roasted ore, while the black line represents the adsorption of oxygen by O_2−Ar-roasted ore).

3.2. XPS Analysis. XPS analysis was conducted on the raw ore, O_2-roasting ore, Ar-roasting ore, and O_2−Ar-roasting ore (Figure 7) to further illustrate the redox mechanism of Ce^{3+}/Ce^{4+} in the respective roasting product. As depicted in Figure 7a, the electron spin magnetic field was coupled with the orbital angular momentum, such that the Ce 3d spin−orbital energy level fell into two spin−orbital energy levels, i.e., Ce $3d_{3/2}$ and Ce $3d_{5/2}$,[27] with a splitting difference of nearly 18.6 eV, while two distinct components controlled each spin−orbital where w' = 905 ± 0.1 eV and w'' = 900 ± 0.1 eV peaks pertain to Ce $3d_{3/2}$. r' = 905 ± 0.1 eV and r'' = 900 ± 0.1 eV peaks can be classified as Ce $3d_{5/2}$. Due to the coupling between O 2p and Ce 4f orbitals (O 2p → Ce 4f electron leap), the final state of $3d^94f^1$ O $2p^6$ resulted in w', r', w'', and r'' as the final state of Ce $3d^94f^2$ O $2p^5$; w', r', w'', and r'' express the characteristic peaks for the presence of Ce^{3+} ions,[28] suggesting that the element Ce in the original ore was primarily present in the +3 valence form. Notably, Ce^{3+} ions did not exhibit the characteristic appearance of the $4f^0$ states.

As depicted in Figure 7b, 10 Ce 3d characteristic peaks appeared in O_2-roasting ore (u' = 916.64 ± 0.1 eV, u'' = 906.6 ± 0.1 eV, u''' = 900.93 ± 0.1 eV, v' = 898.17 ± 0.1 eV, v'' = 887.12 ± 0.1 eV, v''' = 882.63 ± 0.1 eV, w' = 902.67 ± 0.1 eV, w'' = 898.83 ± 0.1 eV, r'' = 884.46 ± 0.1 eV, and r'' = 881.5 ± 0.1 eV).[29] The value of 889 ± 0.1 eV was the Osher peak of Fe (Fe LM6), and w', w'', r', and r''' belonged to the characteristic peaks of Ce^{3+} ions (consistent with the results presented in Figure 5a), The possible reason for this result is from $CePO_4$ (monazite) or attributed to insufficient oxidation. u', u'', u''', v', v'', and v''' belonged to Ce^{4+} ion characteristic peaks.[30] At this time, Ce $3d_{3/2}$ and Ce $3d_{5/2}$ spin orbitals of Ce^{4+} ions were controlled by three characteristic components, where Ce $3d^94f^0$ O $2p^6$, Ce $3d^94f^1$ O $2p^5$, and Ce $3d^94f^2$ O $2p^4$ express $u'(v')$, $u''(v'')$, and $u'''(v''')$ final states and appeared as $4f^0$ final states.[31]

As depicted in Figure 7c, the characteristic peaks of Ce^{3+} and Ce^{4+} appeared in the Ar-roasting ore. Still, the intensity of the characteristic peak of Ce^{4+} was lower than that of Ce^{3+} (1:1.47, Table 2, c). The possible reason for this result is the reaction of Ce^{3+} on the surface with the residual trace O_2 or the decomposition of part of $Ce_3O_4F_3$ to generate CeO_2 and CeF_3

https://doi.org/10.1021/acsomega.4c02088
ACS Omega 2024, 9, 38437−38451

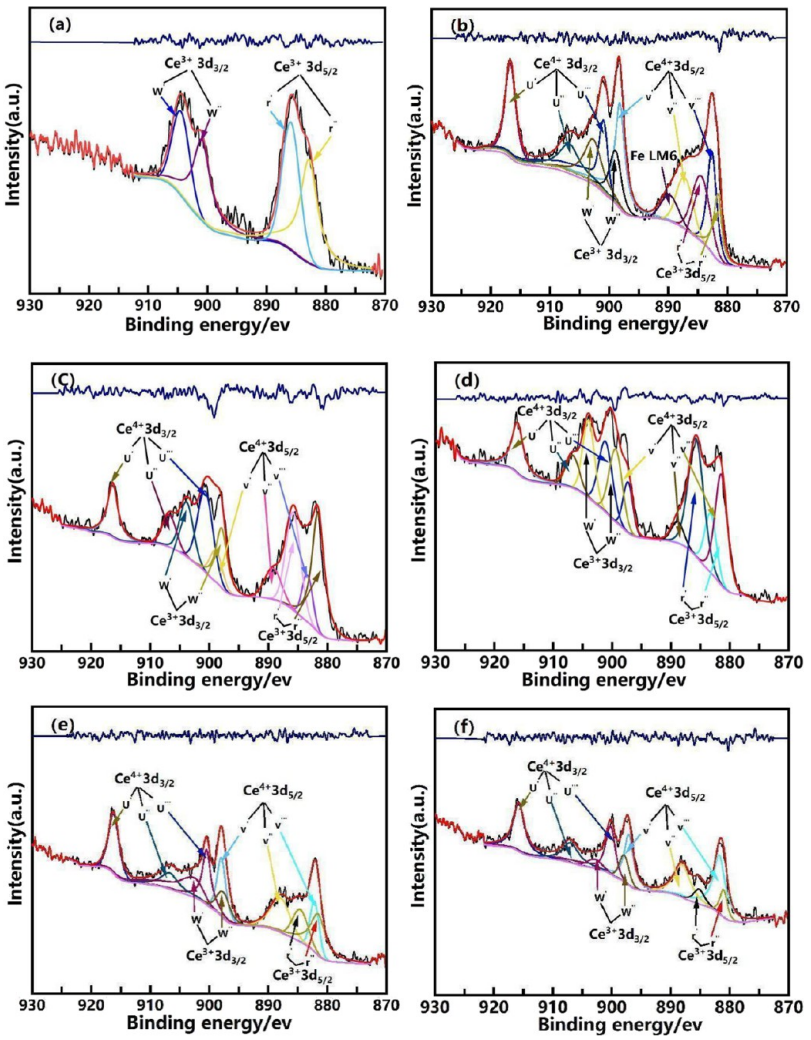

Figure 7. Valence state analysis of the Ce element in different roasted ores: (a) mixed rare earth concentrate, (b) 500 °C O_2-roasted ore, (c) 500 °C Ar-roasted ore, (d) 850 °C Ar-roasted ore, (e) 500 °C O_2−Ar-roasted ore, and (f) 900 °C O_2−Ar-roasted ore.

Table 2. Ratio of the Ce^{4+} to Ce^{3+} 3d Characteristic Peak Area Sum[a]

	A, the sum of the areas of Ce^{4+} 3d peaks, eV	B, the sum of the areas of Ce^{3+} 3d peaks, eV	$\frac{A}{B}$
a		22,242.42	
b	20,930.21	28,876.88	1:1.38
c	17,808.60	26,206.06	1:1.47
d	18,801.20	29,652.90	1:1.58
e	20,684.95	14,378.75	1:0.69
f	24,398.04	4711.32	1:0.19

[a](a) Mixed rare earth concentrate, (b) 500 °C O_2-roasted ore, (c) 500 °C Ar-roasted ore, (d) 850 °C Ar-roasted ore, (e) 500 °C O_2−Ar-roasted ore, and (f) 900 °C O_2−Ar-roasted ore.

(eq 6). When the roasting temperature tended to be increased to 850 °C, the ratio of the sum of characteristic peak areas of Ce^{4+} to the sum of characteristic peak areas of Ce^{3+} increased (1:1.58, Table 2, d), suggesting a weaker reaction of eq 6.

As depicted in Figure 7e,f, the characteristic peaks of Ce^{3+} and Ce^{4+} were also present in the O_2−Ar-roasted ore, whereas the characteristic peaks of Ce^{3+} were primarily from monazite. It is noteworthy that the sum of the characteristic peak areas of Ce^{4+} in the O_2−Ar-roasted ore was significantly higher than that of Ce^{3+} compared with those in the O_2-roasted ore and Ar-roasted ore (1:0.69, Table 2, e), and the sum of the characteristic peak areas of Ce^{4+} was increased significantly with the gradual increase of the oxidation roasting temperature (1:0.19, Table 2, f). The above result suggested that compared with direct oxidation roasting of bastnaesite, the Ar-roasted ore displayed more defects and oxygen vacancies, such that it was also more susceptible to oxidation.

$$Ce_3O_4F_3 \rightarrow 2CeO_2 + CeF_3 \quad (6)$$

The O 1s spectra of different samples in the range of 525−540 eV were analyzed (Figure 8) to further illustrate the role of O_2 in the roasting process of bastnaesite. As depicted in Figure 8a, there were three types of oxygen structures in the mixed rare earth concentrate of Bayan Obo: nonbridging oxygen *K'* (C−O and P−O) centered at 532.2 eV, bridging oxygen *K"* (CO−C and PO−P) centered at 531.3 eV, and 529.8 eV centered on a small amount of lattice oxygen K"' (Ce^{3+}−O),[32−34] where the nonbridging and bridging oxygen primarily originated from the PO_4^{3-} and CO_3^{2-} groups of monazite and bastnaesite. As depicted in Figure 8b, after oxidative roasting at 500 °C, four oxygen structures appeared in the roasted products, comprising nonbridging oxygen *K'* (P−O), bridging oxygen *K"* (PO−P), lattice oxygen *K"'* (Ce^{4+}−O) and adsorbed oxygen M. Simultaneously noting a significant

https://doi.org/10.1021/acsomega.4c02088
ACS Omega 2024, 9, 38437−38451

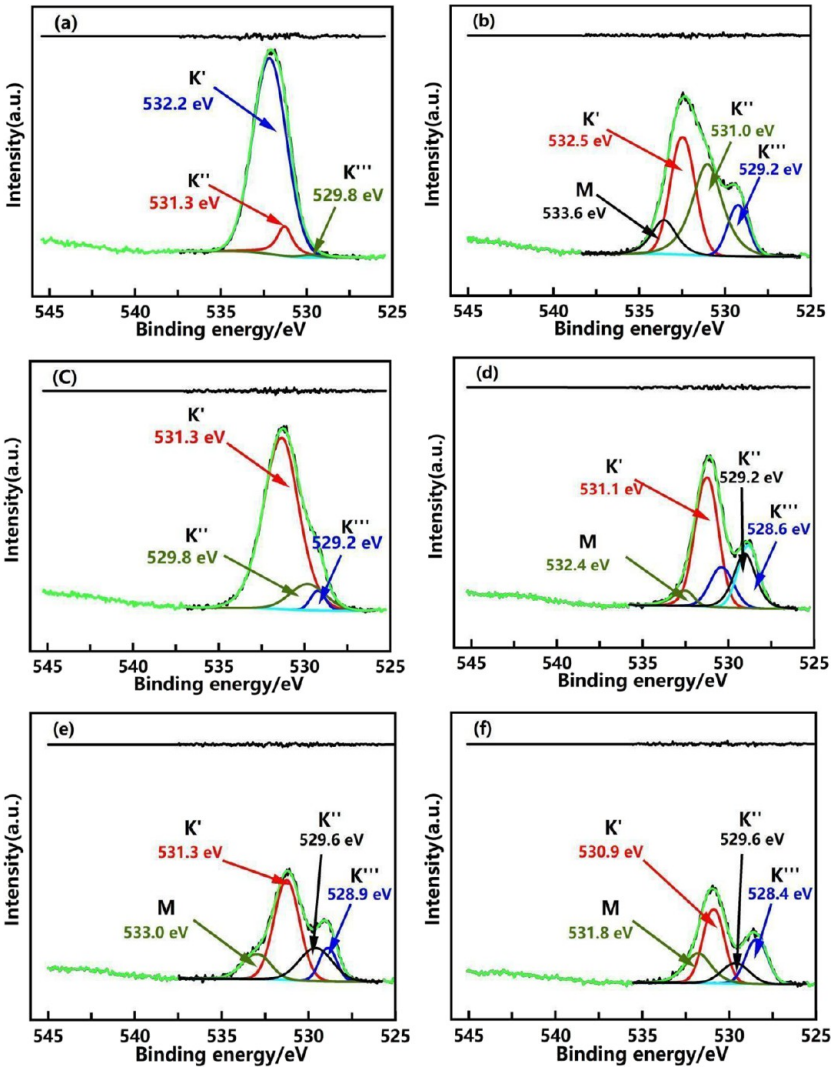

Figure 8. Valence state analysis of the O element in different roasted ores. (a) Mixed rare earth concentrate, (b) 500 °C O_2-roasted ore, (c) 500 °C Ar-roasted ore, (d) 850 °C Ar-roasted ore, (e) 500 °C O_2−Ar-roasted ore, and (f) 900 °C O_2−Ar-roasted ore.

increase in the proportion of bridging oxygen *K*" and lattice oxygen *K*"'.[35,36] The probable reason for the above result is that $REFCO_3$ decomposed when heated, and considerable rare earth phases were generated (e.g., CeOF and CeO_2), resulting in the gradual appearance of the characteristic peak of the lattice oxygen (Ce^{4+}−O). At the same time, $REPO_4$ remains almost unchanged, and the stable presence of the PO_4^{3-} group and the significant reduction of the CO_3^{2-} group lead to the decrease of the bridging oxygen *K*" (PO−P) peaks that gradually appeared. Notably, as indicated by the appearance of the characteristic peak of adsorbed oxygen M, free radical O· started to fill the oxygen vacancies and defects on the mineral surface and caused a Ce^{3+} to Ce^{4+} transition, consistent with the results in Figure 7b.

As depicted in Figure 8c, when the mixed rare earth concentrate was roasted at 500 °C in the Ar atmosphere, the roasted products showed three oxygen structures comprising nonbridging oxygen *K*' (P−O), bridging oxygen *K*" (PO−P), and lattice oxygen *K*"' (Ce^{3+}−O) with similar peak patterns as presented in Figure 7a, whereas no obvious characteristic peak of adsorbed oxygen was identified. When the roasting temperature was increased to 850 °C, a small amount of the characteristic peak of adsorbed oxygen (532.4 eV) appeared. The possible reason for this result is that the residual O_2 or $Ce_3O_4F_3$ decomposed and released part of O atoms. Furthermore, the central peak of lattice oxygen *K*"' (Ce^{3+}−O) shifted toward the low binding energy and the peak intensity increased (Figure 8d), suggesting that the decomposition of $REFCO_3$ was more complete.

As depicted in Figure 8e, when the Ar-roasting ore was oxidatively roasted again, its products also comprised four oxygen structures, namely, nonbridging oxygen *K*' (P−O), bridged oxygen *K*" (PO−P), lattice oxygen *K*"' (Ce^{4+}−O), and adsorbed oxygen M with similar peak patterns to Figure 7b, suggesting that the mineral surface information on Ar-roasted ore after reoxidation roasting was similar to that of O_2-roasted ore. Thus, a theoretical basis was laid for viewing Ar-roasted ore as an intermediate. The peak intensity of the bridging oxygen *K*" (PO−P) was reduced when the roasting temperature was increased to 900 °C, probably because PO_4^{3-} also started to react locally.

3.3. FT-IR Analysis. To gain insights into the change of chemical bonds better during roasting, FT-IR(ATR) analysis was performed on the respective roasting product, as presented in Figure 9 (where υ represents the asymmetric vibration, δ represents the symmetric vibration, γ represents the bending

https://doi.org/10.1021/acsomega.4c02088
ACS Omega 2024, 9, 38437−38451

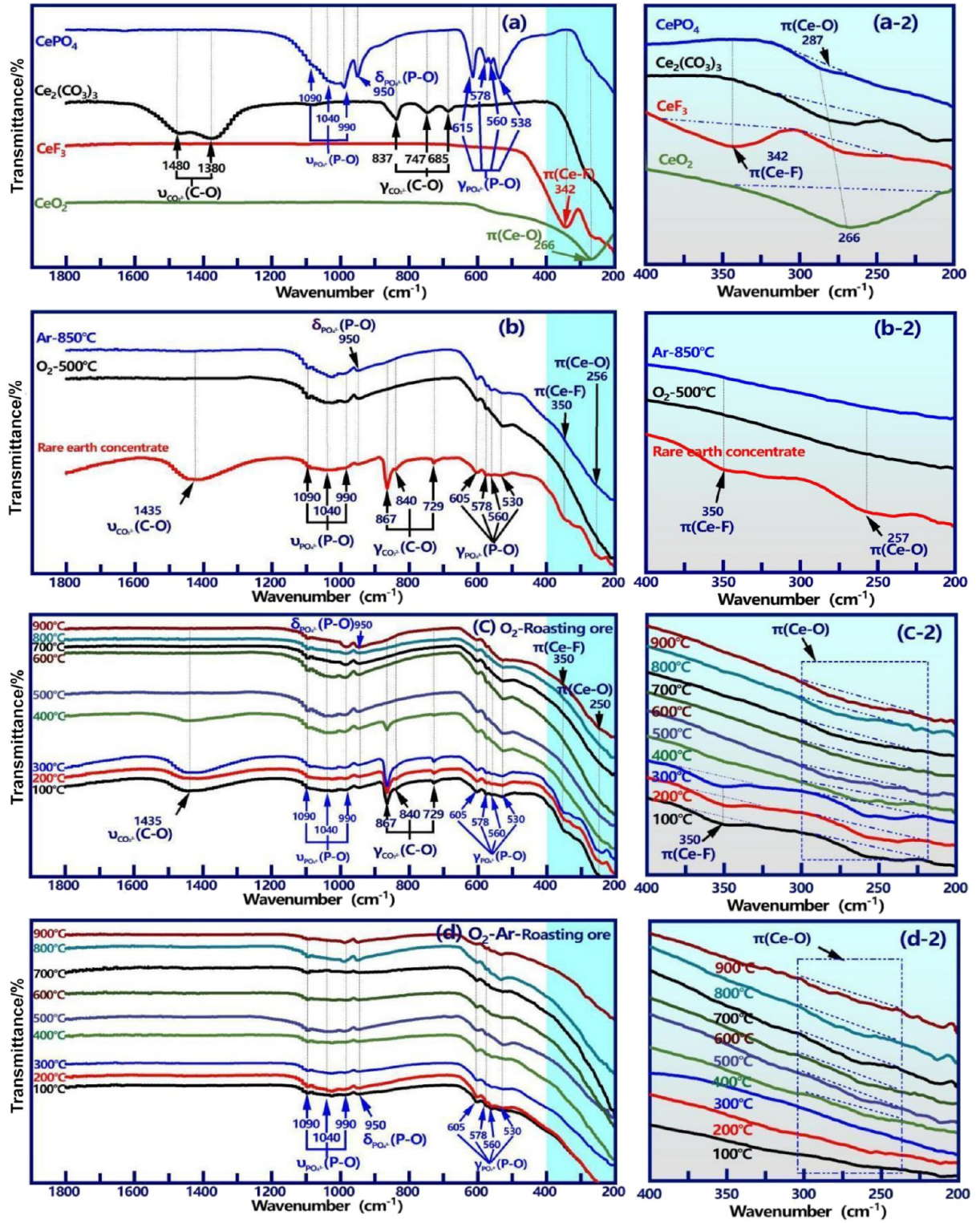

Figure 9. FT-IR(ATR) analysis of (a) pure substance, (b) mixed rare earth concentrate, Ar-roasted ore, and O_2-roasted ore, (c) mixed rare earth ores at different oxidation roasting temperatures, and (d) O_2−Ar-roasted ore at different roasting temperatures.

vibration, and π represents the contraction vibration of the lattice).

The infrared spectra of four chemicals, $CePO_4$, $Ce_2(CO_3)_3$, CeF_3, and CeO_2, were first studied to reasonably determine the breakage of the chemical bonds among the atoms within the rare earth minerals during the roasting process. As depicted in Figure 9a, the characteristic infrared spectra of PO_4^{3-} were mainly asymmetric vibrations υ (1090, 1040, and 990 cm^{-1}), symmetric vibrations δ (950 cm^{-1}), and bending vibrations γ (867, 840, and 729 cm^{-1}). The characteristic infrared spectra of CO_3^{2-} were mainly asymmetric vibrations υ (1435 cm^{-1}) with bending vibrations γ (867, 840, and 729 cm^{-1}). The chemical bonding of CeF_3 and CeO_2 was mainly ionic, and the wavenumbers of their IR characteristic peaks were below 400

https://doi.org/10.1021/acsomega.4c02088
ACS Omega 2024, 9, 38437−38451

cm^{-1}, mainly the contraction vibrations of the lattice π (Ce−F, 342 cm^{-1}) and π (Ce−O, 266 cm^{-1}). Notably, $CePO_4$, $Ce_2(CO_3)_3$, and CeF_3 had a small amount of lattice contraction vibrations π (Ce−O) in the wavenumber range of 287−266 cm^{-1}, suggesting that $CePO_4$ and $Ce_2(CO_3)_3$ were also subjected to some interactions between Ce^{3+} and O^{2-} during molecular conformation, while CeF_3 was probably attributed to air oxidation or contamination from the preparation process.

As depicted in Figure 9b, in the wavenumber range of 1800−400 cm^{-1}, no matter what type of atmosphere the mixed rare earth concentrate was roasted in, the peak strength of the asymmetric vibration υ and the bending vibration γ of CO_3^{2-} was reduced to varying degrees, whereas the asymmetric vibration υ, symmetric vibration δ, and bending vibration γ peak of PO_4^{3-} did not vary notably. In the wavenumber range of 400−200 cm^{-1}, trace amounts of lattice contraction vibrations π (Ce−F and Ce−O) were still visible in the 850 °C Ar-roasted ore, whereas the lattice contraction vibrations π (Ce−O, 257 cm^{-1}) became more significant in the O_2-roasted ore. The possible reason for the above result is that during the thermal decomposition of the mixed rare earth concentrate, the CO_3^{2-} group in $REFCO_3$ first decomposed (eq 1) to produce the REOF phase and CO_2, and the contraction vibration of π(Ce−F) was more vigorous. Afterward, with the continuous intervention of O_2, the free radical O· was adsorbed to the remaining oxygen vacancies and lattice defect sites on the surface of REOF minerals such that the contraction vibration of π(Ce−O) was strengthened, while the contraction vibration of π(Ce−F) was masked. This trend became more significant with the gradual increase of the roasting temperature (Figure 9c). It is worth noting that the intensity of the π(Ce−O) characteristic peak in the low-temperature stage (100−400 °C) is stronger than that in the high-temperature stage (500−900 °C), which can be attributed to the fact that most of the $REFCO_3$ is not yet decomposed during the low-temperature stage. Indeed, a small amount of fluorine escape may be one of the reasons for the reduction of the π(Ce−F) lattice shrinkage vibration. In this process, $REPO_4$ was relatively stable and hardly varied, such that the asymmetric vibration υ, symmetric vibration δ, and bending vibration γ peaks of PO_4^{3-} were always present.

As depicted in Figure 9d, the characteristic peak pattern was essentially the same in the wavenumber range of 1800−400 cm^{-1} with the gradual increase of the roasting temperature. In the wavenumber range of 400−200 cm^{-1}, the contraction vibration π(Ce−F) of the lattice was almost undetectable, suggesting that the adsorption of radical O· can be achieved at low temperatures for Ar-roasted ores. In contrast, the contraction vibration of π(Ce−O) was slightly enhanced with increasing temperature, consistent with the previous findings in Figure 9b,c. In brief, in addition to the calcination temperature, O_2 may be one of the inducing factors that promote the escape of a small amount of F atoms.

3.4. TEM Analysis. As depicted in Figure 10b, the diffraction ring spacing of each crystal plane of Ar-roasted ore was similar to that of the (La, Ce)OF (PDF no. 00-057-0608). The above result suggested that while the F element played a significant role in $Ce_3O_4F_3$ bonding (Figure 10a,c), the O_2-roasted ore and O_2−Ar-roasted ore diffraction ring of each crystal plane spacing was closer to that of CeO_2 (PDF no. 03-065-2975), whereas O_2-roasted ore had (200) crystal planes protruded out in the O_2-roasted ore. The possible reason for

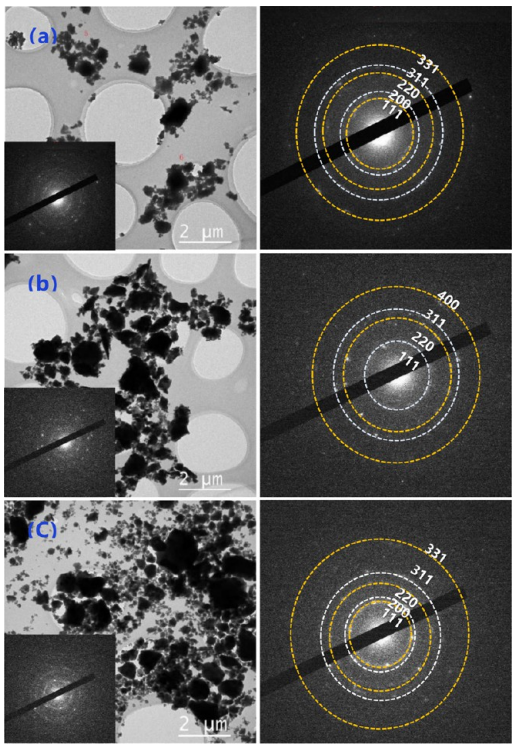

Figure 10. TEM analysis ((a) O_2−Ar-roasted ore, (b) Ar-roasted ore, and (c) O_2-roasted ore).

this result is the different degree of oxidation of Ce^{3+} to Ce^{4+}, consistent with the results in Figure 3. Thus, it was assumed that the Ar atmosphere-roasted ore (CeO_xF) was an intermediate product of $REFCO_3$ in the oxidative roasting process, and the main physical phase change that occurred was expressed as $CeFCO_3 \rightarrow CeO_xF \rightarrow CeO_x$.

3.5. Fluorine Loss during Thermal Decomposition. The gases of the Ar-roasting ore oxidation process were analyzed (Figure 11) to further investigate the possible reaction processes during the roasting of bastnaesite. As indicated by the result, with the gradual increase of the roasting temperature, the content of O_2 tended to decline, arising from the adsorption of O_2 on the mineral surface (consistent with the results in Figure 6). Moreover, trace amounts of F_2 were produced. The fluorine escape behavior of the mixed rare earth concentrate at different roasting temperatures was examined to investigate the cause of F_2 production. As depicted in Figure 12, with the gradual increase of the roasting temperature (100−700 °C), the fluorine loss rate was between 5 and 6%, while most of the fluorine was still present in the mineral. As depicted in Figure 13, the difference in chemical bonds shifted between the F 1s central peak of the mixed rare earth concentrate, and different roasted ores were within 0.5 eV, suggesting that a higher energy was required for the chemical bond breakage of fluorine. To verify this conjecture, the morphology and elemental distribution states of the mixed rare earth concentrate during high-temperature roasting were analyzed, as presented in Figures 14 and 15 and Table 3.

Figure 14 illustrates that as the roasting temperature increases, the La, P, and O elements exhibit a strip-like structure and gradually accumulate together, while the Ce element gradually accumulates with Ca, F, and O elements. At temperatures exceeding 1200 °C, spherical ceria particles with a diameter of approximately 1.0 μm begin to form (Figure 15).

https://doi.org/10.1021/acsomega.4c02088
ACS Omega 2024, 9, 38437−38451

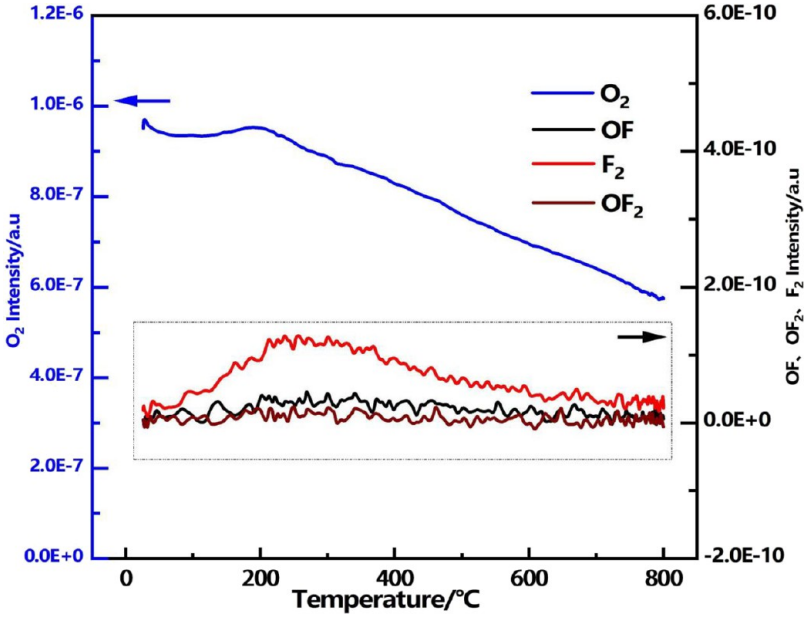

Figure 11. Thermal decomposition gas analysis.

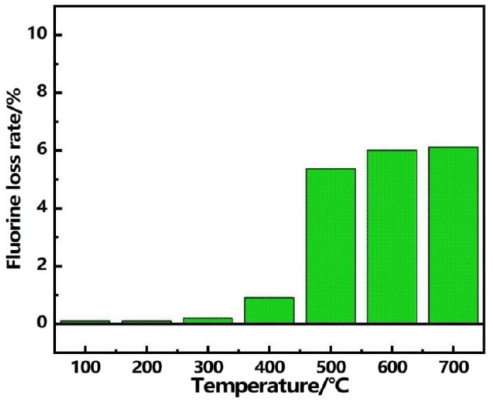

Figure 12. Loss rate of fluorine (loss rate of F in mixed rare earth concentrate at different roasting temperatures).

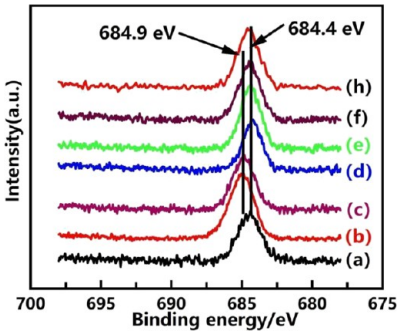

Figure 13. F 1s XPS. (a) Mixed rare earth concentrate, (b) 500 °C O_2-roasted ore, (c) 500 °C Ar-roasted ore, (d) 850 °C Ar-roasted ore, (e) 500 °C O_2−Ar-roasted ore, (f) 900 °C O_2−Ar-roasted ore, and (h) 1400 °C O_2-roasted ore.

The size of the spherical particles increases with the calcination temperature. Table 3 illustrates that as the roasting temperature increases (1100−1500 °C), the F content in ceria spherical particles declines from 12.18 to 0.89%, while the O content rises from 4.96 to 11.00%. In comparison to the low-temperature calcination process (100−700 °C) (Figure 12), the high-temperature calcination method is more conducive to the escape of fluorine.

In brief, F_2 may originate from the mineral surface due to the presence of unsaturated bonds in a small amount of F· on the mineral surface (Figure 16) and the relatively low energy required for the reaction between O· and F·, which can easily react to form OF· and OF_2 (eqs 7 and 8). In addition, OF_2 can decompose to O_2 and F_2 at 200 °C (eq 9).[37]

$$O\cdot + F\cdot \rightarrow OF\cdot \quad (7)$$

$$FO\cdot + F\cdot \rightarrow O_{F_2} \quad (8)$$

$$2FO_2 \rightarrow O_2 + 2F_2 \quad (9)$$

3.6. Roasting Reaction Mechanism. The possible reaction pathways of bastnaesite during roasting decomposition were deduced based on the above data analysis (Figure 17). As indicated by the result, the bond energy of ⑥C═O (σ bond and π bond) in CO_3^{2-} exceeded that of ① or ②C−O (σ bond). On that basis, with the gradual increase of the roasting temperature, the polarization of C and O elements in CO_3^{2-} intensified. Subsequently, Ce^{3+} preferentially seized an O^{2-} in CO_3^{2-} bonded by an σ bond, leading to the breakage of the ① or ②C−O bond. For convenience, it was assumed that the ①C−O bond occurred first, and the Ce-O·$^-$ (a p orbital electron) and C·$^-$ (an sp^2 orbital) had an unpaired electron after the break, which tend to form Ce═O and C═O. Moreover, the breakage of ①C−O caused electron rearrangement and site resistance effects, resulting in further elongation and weakening of the ④Ce−O bond, and the Ce-O·$^-$ bond length was shortened, such that ④Ce−O started to display a trend of breaking. Afterward, two reaction pathways were identified next. (1) When O_2 was present, the high-temperature thermal radiation caused the chemical bond of O_2 to break evenly, producing radical O· ($O_2 + h\nu$ (180−240 nm) → 2O·), which competed with O^{2-} in the ④Ce−O bond for the 6s5d orbital electrons of Ce^{3+} and eventually attracted the p orbital electrons of O^{2-} in the ④Ce−O bond to form a π bond. As a result, a lower reaction potential and decomposition

https://doi.org/10.1021/acsomega.4c02088
ACS Omega 2024, 9, 38437−38451

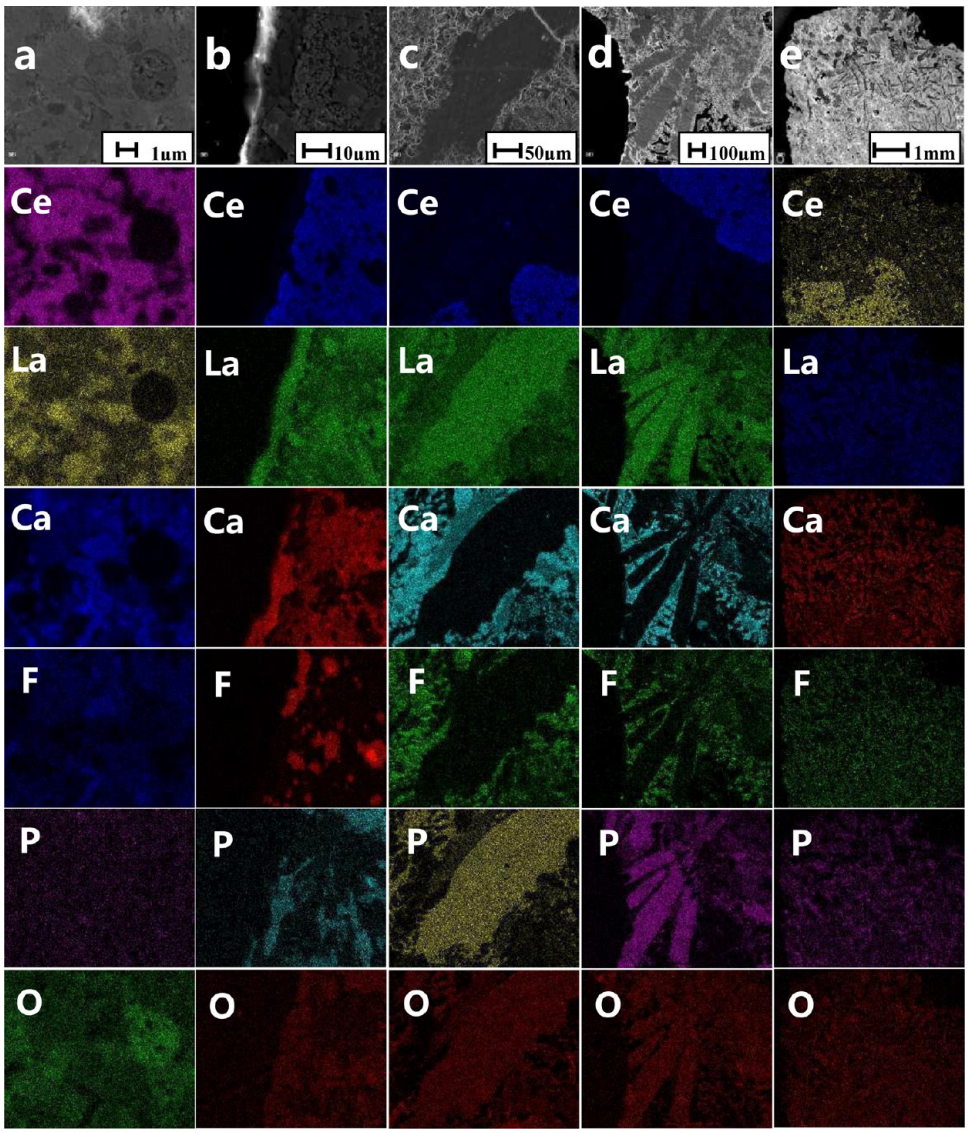

Figure 14. Face scan (surface scanning of mixed rare earth concentrates at different roasting temperatures) ((a) 1100, (b) 1200, (c) 1300, (d) 1400, and (e) 1500 °C).

temperature were achieved, such that the breakage of the ④Ce−O bond was facilitated to produce CO_2 gas. Moreover, due to the change of the charge field, the 4f electron shielding effect was reduced, and 4f electrons started to participate in bonding, such that the valence state of Ce in the main phase $Ce_{11}O_{20}$ of O_2-roasting ore had an average state of +3.32. (2) When Ar was present, the fracture of ④Ce−O should give higher energy to generate the $Ce_3O_4F_3$ phase due to the lack of active oxidant radical O· attraction. Thus, the temperature of complete decomposition of CO_3^{2-} in Ar-roasting ore was higher than that of the O_2-roasting ore, consistent with the results in Figure 4. (3) When the obtained Ar-roasting ore was roasted and oxidized again or in the presence of residual O_2, the radical O· generated by the high-temperature thermal radiation first attracted 4f orbital electrons to generate a structure similar to $Ce_3O_4F_3$. The above-mentioned process was shown as a weight gain phenomenon, accompanied by the oxidation behavior of Ce, consistent with the results in Figure 4. Afterward, the molecular vibration intensified with the gradual increase of the roasting temperature (≥800 °C). The ⑤Ce−F bond started to be elongated and weakened, whereas the mutual gravitational force between the valence level electrons of the radical O· and the F element was strengthened. In addition, the attraction and competition with the O atom for the 6s5d orbital electrons of Ce were enhanced, such that the ⑤Ce−F bond was broken. Subsequently, protons and neutrons were transferred to generate the Ce_7O_{12} phase and intermediate $OF\cdot^-$, such that a weight loss phenomenon was generated. Due to the lively chemical nature of intermediate $OF\cdot^-$, it continued to combine with $F\cdot^-$ to generate O_2F, whereas the molecular mass of the O_2F was larger than that of Ar molecules and easy to decompose. On that basis, it continued to decompose at the bottom to generate F_2 and O_2 (eq 9), and the generation of O_2 was the cause of partial oxidation of the minerals at the bottom during the Ar-roasting process, which is the reason why the oxidation phenomenon at the bottom in Figure 1 was generally significant. Nevertheless, intermediates, O_2F and $OF\cdot^-$, and F_2 were adsorbed on the mineral surface due to their lively chemical properties, which is also the reason why the weight loss rate fluctuated up and down.

https://doi.org/10.1021/acsomega.4c02088
ACS Omega 2024, 9, 38437−38451

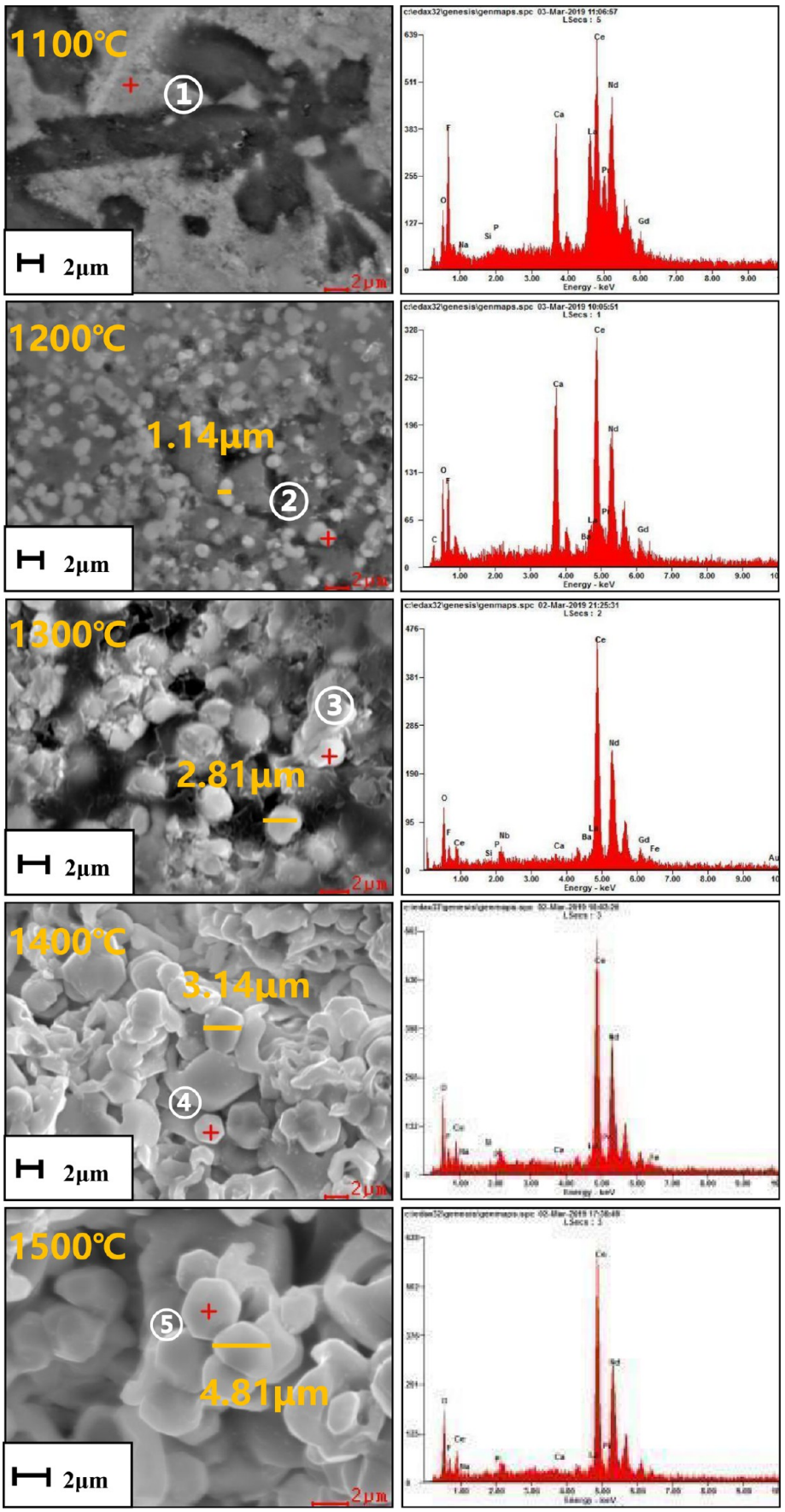

Figure 15. SEM-EDS (morphology and energy spectrum of mixed rare earth concentrates at high-temperature roasting temperatures).

https://doi.org/10.1021/acsomega.4c02088
ACS Omega 2024, 9, 38437−38451

Table 3. EDS Pattern of Roasted Ore

	temperature	La	Ce	Ca	P	F	O
①	1100 °C	20.03%	36.66%	6.06%	0.78%	12.18%	4.96%
②	1200 °C	5.99%	45.68%	8.94%	0.71%	10.44%	10.32%
③	1300 °C	3.71%	65.73%	0.71%	0.45%	0.82%	8.36%
④	1400 °C	3.65%	69.14%	0.43%	0.47%	0.37%	10.64%
⑤	1500 °C	3.17%	72.45%	0.66%	0.78%	0.89%	11.00%

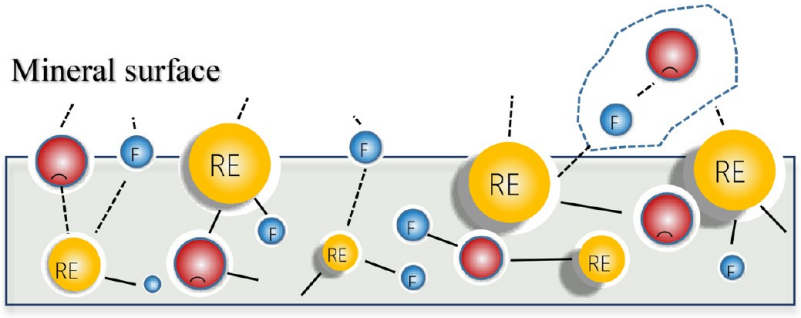

Figure 16. Mechanism of fluorine escape.

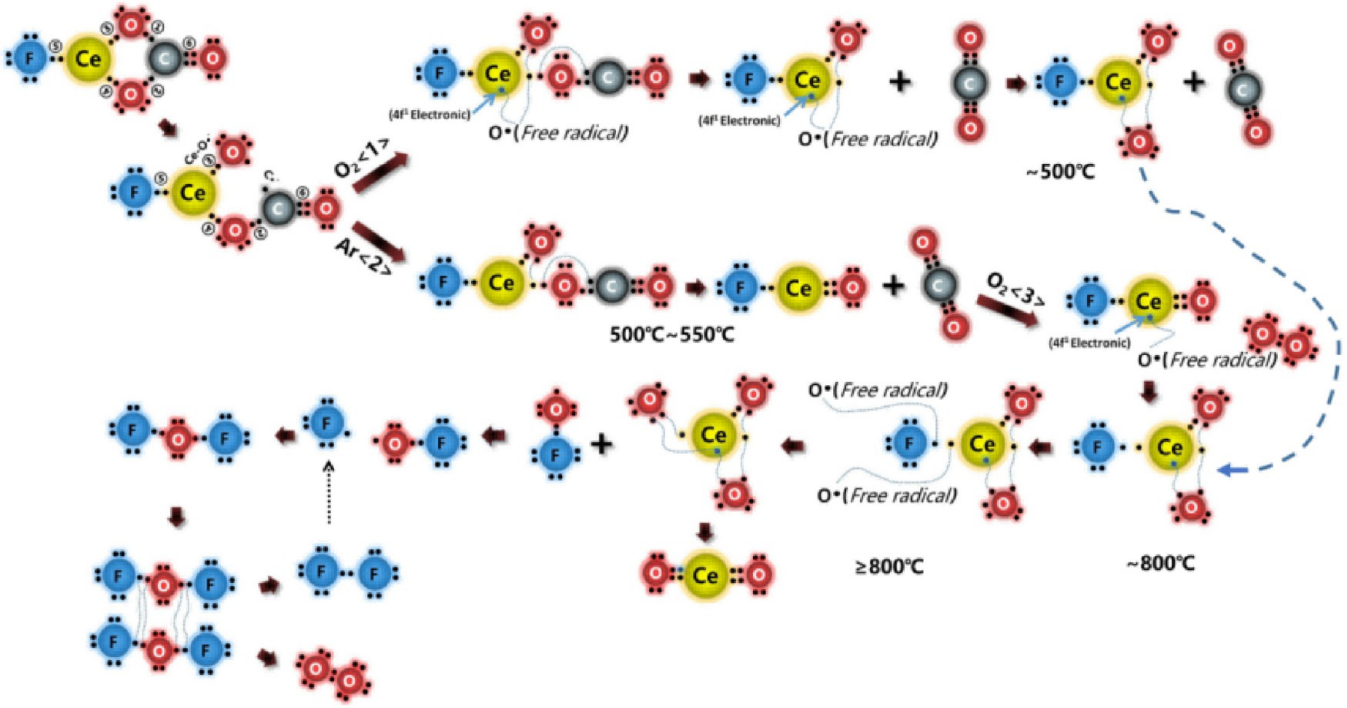

Figure 17. Mechanism of the roasting reaction of bastnaesite.

4. CONCLUSIONS

Regardless of the roasting atmosphere, monazite ($REPO_4$) almost did not vary notably, whereas the model of thermal decomposition of bastnaesite primarily fell into two stages. At the first stage, bastnaesite was subjected to first decomposition to generate REOF and CO_2, and considerable oxygen vacancies and lattice defects were generated, while the free radical O· began to adsorb and escape on its mineral surface, thus facilitating the transformation of Ce^{3+} to Ce^{4+}. Since the sum of CO_2 loss and free radical O· escape at this stage was much larger than the free radical O· adsorption, this stage finally displayed the trend of weight loss. At the second stage, with the gradual increase of the roasting temperature (800−1000 °C), the vibration of the REOF lattice was increased, which led to the decrease of oxygen storage and the release capacity of REOF minerals while strengthening the gravitational force between radical O· and F· atoms. Lastly, the atoms escaped in the form of OF_2, which continuously decomposed to generate F_2 and O_2. Due to the weak reaction of OF_2 generation and the small amount of free radical O· escape from REOF minerals themselves, the weight loss at this stage reached only 0.74%. The roasting model is capable of successfully explaining some macroscopic phenomena in the roasting decomposition of mixed rare earth minerals in Bayan Obo, revealing its essential laws from a microscopic perspective. This model also explains part of the reaction

https://doi.org/10.1021/acsomega.4c02088
ACS Omega 2024, 9, 38437−38451

mechanism of other models and has been more extensively applied with some theoretical innovation.

AUTHOR INFORMATION

Corresponding Author

Zhaogang Liu − *School of Rare Earth Industry, Inner Mongolia University of Science and Technology, Baotou, Inner Mongolia 014010, China; Key Laboratory of Green Extraction and Efficient Utilization of Light Rare Earth Resources, Ministry of Education, Baotou, Inner Mongolia 014010, China; Key Laboratory of Rare Earth Wet Metallurgy and Light Rare Earth Applications of Inner Mongolia Autonomous Region, Baotou, Inner Mongolia 014010, China; School of Materials and Metallurgy, Inner Mongolia University of Science and Technology, Baotou 014010, China;* orcid.org/0000-0003-4670-1403; Email: liuzg65@163.com

Authors

Jianfei Li − *School of Rare Earth Industry, Inner Mongolia University of Science and Technology, Baotou, Inner Mongolia 014010, China; Key Laboratory of Green Extraction and Efficient Utilization of Light Rare Earth Resources, Ministry of Education, Baotou, Inner Mongolia 014010, China; Key Laboratory of Rare Earth Wet Metallurgy and Light Rare Earth Applications of Inner Mongolia Autonomous Region, Baotou, Inner Mongolia 014010, China; School of Metallurgical and Ecological Engineering, University of Science and Technology Beijing, Beijing 100083, China*

Yubo Xu − *School of Rare Earth Industry, Inner Mongolia University of Science and Technology, Baotou, Inner Mongolia 014010, China; Key Laboratory of Green Extraction and Efficient Utilization of Light Rare Earth Resources, Ministry of Education, Baotou, Inner Mongolia 014010, China; Key Laboratory of Rare Earth Wet Metallurgy and Light Rare Earth Applications of Inner Mongolia Autonomous Region, Baotou, Inner Mongolia 014010, China*

Xiaowei Zhang − *School of Rare Earth Industry, Inner Mongolia University of Science and Technology, Baotou, Inner Mongolia 014010, China; Key Laboratory of Green Extraction and Efficient Utilization of Light Rare Earth Resources, Ministry of Education, Baotou, Inner Mongolia 014010, China; Key Laboratory of Rare Earth Wet Metallurgy and Light Rare Earth Applications of Inner Mongolia Autonomous Region, Baotou, Inner Mongolia 014010, China*

Jinxiu Wu − *School of Rare Earth Industry, Inner Mongolia University of Science and Technology, Baotou, Inner Mongolia 014010, China; Key Laboratory of Green Extraction and Efficient Utilization of Light Rare Earth Resources, Ministry of Education, Baotou, Inner Mongolia 014010, China; Key Laboratory of Rare Earth Wet Metallurgy and Light Rare Earth Applications of Inner Mongolia Autonomous Region, Baotou, Inner Mongolia 014010, China*

Zhisheng Dong − *School of Rare Earth Industry, Inner Mongolia University of Science and Technology, Baotou, Inner Mongolia 014010, China*

Xiaoyan Hao − *China North Rare Earth (Group) High Tech Co., Ltd., Baotou, Inner Mongolia 014010, China*

Complete contact information is available at: https://pubs.acs.org/10.1021/acsomega.4c02088

Notes

The authors declare no competing financial interest.

ACKNOWLEDGMENTS

This work was financially supported by the Inner Mongolia Autonomous Region Natural Science Foundation(2022QN05017) and the National Natural Science Foundation of China (51964040). Thanks to the support of the Scientific Research Fund for the Introduction of High-Level Talents (Jianfei Li) to Institutions of the Inner Mongolia Autonomous Region (research on the oxidation/sodium leaching strategy of mixed rare earth ore and key technologies for synergistic low-carbon disposal of "three wastes").

REFERENCES

(1) Shuai, J.; Zhao, Y.; Shuai, C.; Wang, J.; Yi, T.; Cheng, J. Assessing the International Co-Opetition Dynamics of Rare Earth Resources between China, USA, Japan and the EU: An Ecological Niche Approach. *Resour. Policy* **2023**, *82*, No. 103446.

(2) Gupta, S. K.; Zuniga, J. P.; Abdou, M.; Thomas, M. P.; De Alwis Goonatilleke, M.; Guiton, B. S.; Mao, Y. Lanthanide-Doped Lanthanum Hafnate Nanoparticles as Multicolor Phosphors for Warm White Lighting and Scintillators. *Chem. Eng. J.* **2020**, *379*, No. 122314.

(3) Saidi, F.; Mokhdar, S.; Dergal, M.; Ammaria, M.; Kallekh, A.; Abd El-Gawad, H. H. Ab Initio Study of the Structural, Electronic, Magnetic, Mechanical, Optical, and Dynamical Properties of the Rare-Earth Dihydrides MH_2 (M= Yb, Sc, Eu, Y, Lu and Gd). *Vacuum* **2023**, No. 112011.

(4) Xu, L.; Wen, X.; Xu, C.; Bian, Y.; Chen, M.; Cheng, G.; Wu, C.; Qiu, J.; Chen, B.; Hu, X. Rare Earths Modified Highly Dispersed Fibrous Ni/KCC-1 Nanosphere Catalysts with Superb Low-Temperature CO_2 Methanation Performances. *Appl. Surf. Sci.* **2023**, *608*, No. 155258.

(5) Guo, L.; Mu, Z.; Da, P.; Weng, Z.; Xi, P.; Yan, C.-H. Hollow Structures with Rare Earths: Synthesis and Electrocatalytic Applications. *EnergyChem.* **2022**, *4* (5), No. 100088.

(6) Whitty-Léveillé, L.; Reynier, N.; Larivière, D. Rapid and Selective Leaching of Actinides and Rare Earth Elements from Rare Earth-Bearing Minerals and Ores. *Hydrometallurgy* **2018**, *177*, 187−196.

(7) Wang, L.; Huang, X.; Yu, Y.; Zhao, L.; Wang, C.; Feng, Z.; Cui, D.; Long, Z. Towards Cleaner Production of Rare Earth Elements from Bastnaesite in China. *J. Clean. Prod.* **2017**, *165* (2), 231−242.

(8) Cen, P.; Bian, X.; Liu, Z.; Gu, M.; Wu, W.; Li, B. Extraction of Rare Earths from Bastnaesite Concentrates: A Critical Review and Perspective for the Future. *Miner. Eng.* **2021**, *171*, No. 107081.

(9) Cen, P.; Bian, X.; Wu, W.; Li, B. A Sustainable Green Technology for Separation and Simultaneous Recovery of Rare Earth Elements and Fluorine in Bastnaesite Concentrates. *Sep. Purif. Technol.* **2021**, *274*, No. 118380.

(10) Zhao, J.; Pan, F.; Liu, H. An Environmental Friendly Na_2CO_3-Roasting Decomposition Strategy for the Mixed Rare Earth Concentrate. *Sep. Purif. Technol.* **2016**, *168*, 161−167.

(11) Zhang, Y.; Xu, Y.; Huang, X.; Long, Z.; Cui, D.; Hu, F. Study on Thorium Recovery from Bastnaesite Treatment Process. *J. Rare Earths* **2012**, *30* (4), 374−377.

(12) Li, M.; Zhang, D.; Yan, Y.; Gao, K.; Liu, X.; Li, J. Effect of Oxidation Behavior of Cerium during the Roasting Process on the Leaching of Mixed Rare Earth Concentrate. *Hydrometallurgy* **2017**, *174* (March), 156−166.

(13) Wang, L. S.; Yu, Y.; Huang, X. W.; Long, Z. Q.; Cui, D. L. Toward greener comprehensive utilization of bastnaesite: Simultaneous recovery of cerium, fluorine, and thorium from bastnaesite

leach liquor using HEH(EHP). *Chem. Eng. J.* **2013**, *215*−*216*, 162−167.
(14) Zhang, D.; Li, M.; Gao, K.; Li, J.; Yan, Y.; Liu, X. Ultrasonics - Sonochemistry Physical and Chemical Mechanism Underlying Ultrasonically Enhanced Hydrochloric Acid Leaching of Non-Oxidative Roasting of Bastnaesite Bastnaesite/Mixed Rare Earth Non-Oxidation Roasting Leaching with HCl Solution of $RECl_3$ F. *Ultrason. - Sonochemistry* **2017**, *39* (May), 774−781.
(15) García, A. C.; Latifi, M.; Chaouki, J. Kinetics of Calcination of Natural Carbonate Minerals. *Miner. Eng.* **2020**, *150*, No. 106279.
(16) Li, J.; Li, M.; Zhang, D.; Gao, K.; Xu, W.; Wang, H.; Geng, J.; Ma, X.; Huang, L. Clean Production Technology of Selective Decomposition of Bayan Obo Rare Earth Concentrate by NaOH. *J. Clean. Prod.* **2019**, *236*, No. 117616.
(17) Gysi, A. P.; Williams-Jones, A. E. The Thermodynamic Properties of Bastnäsite-(Ce) and Parisite-(Ce). *Chem. Geol.* **2015**, *392*, 87−101.
(18) Sinclair, L. K.; Baek, D. L.; Thompson, J.; Tester, J. W.; Fox, R. V. Rare Earth Element Extraction from Pretreated Bastnäsite in Supercritical Carbon Dioxide. *J. Supercrit. Fluids* **2017**, *124*, 20−29.
(19) Montes-Hernandez, G.; Chiriac, R.; Findling, N.; Toche, F.; Renard, F. Synthesis of Ceria ($CeO_2$and CeO_{2-x}) Nanoparticles via Decarbonation and Ce(III) Oxydation of Synthetic Bastnäsite ($CeCO_3F$). *Mater. Chem. Phys.* **2016**, *172*, 202−210.
(20) Montes-Hernandez, G. Synthesis of Magnetite, Ceria and Magnetite-Ceria Materials by Calcination of Nanostructured Precursor-Minerals. *Mater. Lett.* **2020**, *276*, No. 128246.
(21) Zhao, L.; Wang, L.; Shuai, G.; Long, Z.; Cui, D.; Huang, X. Thermal Decomposition and Oxidation of Bastnaesite Concentrate in Inert and Oxidative Atmosphere. *J. Rare Earths* **2018**, *36* (7), 758−764.
(22) Li, J.; Li, M.; Zhang, D.; Gao, K.; Xu, W.; Wang, H.; Geng, J.; Huang, L. Clean Production Technology of Baiyun Obo Rare Earth Concentrate Decomposed by $Al(OH)_3$-NaOH. *Chem. Eng. J.* **2020**, *382*, No. 122790.
(23) Zou, D.; Chen, J.; Hu, J.; Li, K.; Li, D. Thermal Decomposition Mechanism of Low-Content-Fluorite Bayan Obo Rare Earth Concentrate Roasted with Sodium Carbonate and Its Consequent Separation Study. *J. Rare Earths* **2020**, *38* (9), 994−1002.
(24) Wheeler, D. W. Kinetics and Mechanism of the Oxidation of Cerium in Air at Ambient Temperature. *Corros. Sci.* **2016**, *111*, 52−60.
(25) Bo, Q.; Meng, F.; Wang, L. Facile Hydrothermal Synthesis of CeO_2 Nano-Octahedrons and Their Magnetic Properties. *Mater. Lett.* **2014**, *133*, 216−219.
(26) Deng, J.; Li, S.; Xiong, L.; Wang, J.; Yuan, S.; Chen, Y. Different Thermal Behavior of Nanostructured CeO_2-ZrO_2 Based Oxides with Varied Ce/Zr Molar Ratios. *Mater. Chem. Phys.* **2019**, *236*, No. 121767.
(27) Grabchenko, M. V.; Mamontov, G. V.; Zaikovskii, V. I.; La Parola, V.; Liotta, L. F.; Vodyankina, O. V. The Role of Metal−Support Interaction in Ag/CeO_2 Catalysts for CO and Soot Oxidation. *Appl. Catal. B Environ.* **2020**, *260*, No. 118148.
(28) Bêche, E.; Charvin, P.; Perarnau, D.; Abanades, S.; Flamant, G. Ce 3d XPS Investigation of Cerium Oxides and Mixed Cerium Oxide (CexTiyOz). *Surf. Interface Anal.* **2008**, *40* (3−4), 264−267.
(29) Hussain, S.; Aslam, N.; Yang, X.; Javed, M. S.; Xu, Z.; Wang, M.; Liu, G.; Qiao, G. Unique Polyhedron CeO_2 Nanostructures for Superior Formaldehyde Gas-Sensing Performances. *Ceram. Int.* **2018**, *44* (16), 19624−19630.
(30) Dong, H.; Zhang, L.; Li, L.; Deng, W.; Hu, C.; Zhao, Z.; Gong, J. Abundant Ce^{3+} Ions in Au-CeO_x Nanosheets to Enhance CO_2 Electroreduction Performance. *Small* **2019**, *15* (17), 1900289.
(31) Liu, J.; Dou, Z.; Zhang, T. Preparation of Oxygen Vacancy-Controllable CeO2 by Electrotransformation of a $CeCl_3$ Solution and Its Oxidation Mechanism. *Ceram. Int.* **2020**, *46* (5), 5976−5982.
(32) Yu, X.; Wu, X.; Chen, Z.; Huang, Z.; Jing, G. Oxygen Vacancy Defect Engineering in Mn-Doped CeO_2 Nanostructures for Nitrogen Oxides Emission Abatement. *Mol. Catal.* **2019**, *476*, No. 110512.
(33) Paparazzo, E. XPS Studies of Damage Induced by X-Ray Irradiation on CeO_2 Surfaces. *Surf. Sci.* **1990**, *234* (1−2), L253−L258.
(34) Zeng, Y.; Wang, Y.; Zhang, S.; Zhong, Q.; Rong, W.; Li, X. One-Pot Synthesis of Ceria and Cerium Phosphate (CeO_2-$CePO_4$) Nanorod Composites for Selective Catalytic Reduction of NO with NH_3: Active Sites and Reaction Mechanism. *J. Colloid Interface Sci.* **2018**, *524*, 8−15.
(35) Choudhary, S.; Sahu, K.; Bisht, A.; Singhal, R.; Mohapatra, S. Template-Free and Surfactant-Free Synthesis of CeO_2 Nanodiscs with Enhanced Photocatalytic Activity. *Appl. Surf. Sci.* **2020**, *503*, No. 144102.
(36) Yang, C.; Zhang, K.; Zhang, Y.; Peng, G. jian; Yang, M.; Wen, J.; Xie, Y.; Xia, F.; Jia, L.; Zhang, Q. An Environmental and Highly Active Ce/Fe-Zr-SO2- 4 Catalyst for Selective Catalytic Reduction of NO with NH_3: The Improving Effects of CeO_2 and SO2- 4. *J. Environ. Chem. Eng.* **2021**, *9* (6), No. 106799.
(37) Behnam Azad, B.; Ashique, R.; Chirakal, R.; Schrobilgen, G. J. Selective Fluorination of M-Tyrosine by OF_2. *J. Fluor. Chem.* **2008**, *129* (1), 22−27.

https://doi.org/10.1021/acsomega.4c02088
ACS Omega 2024, 9, 38437−38451